2008

A high-order triangular discontinuous Galerkin oceanic shallow water model

Giraldo, F.X.; Warburton, T.

Giraldo, F.X. & Warburton, T. 2008, "A high-order triangular discontinuous Galerkin oceanic shallow water model", International Journal for Numerical Methods in Fluids, vol. 56, no. 7, pp. 899-925.
https://hdl.handle.net/10945/56992

INTERNATIONAL JOURNAL FOR NUMERICAL METHODS IN FLUIDS
Int. J. Numer. Meth. Fluids 2008; **56**:899–925
Published online 10 July 2007 in Wiley InterScience (www.interscience.wiley.com). DOI: 10.1002/fld.1562

A high-order triangular discontinuous Galerkin oceanic shallow water model

F. X. Giraldo[1,*,†] and T. Warburton[2]

[1]*Department of Applied Mathematics, Naval Postgraduate School, Monterey, CA 93943, U.S.A.*
[2]*Computational and Applied Mathematics, Rice University, Houston, TX 77005, U.S.A.*

SUMMARY

A high-order triangular discontinuous Galerkin (DG) method is applied to the two-dimensional oceanic shallow water equations. The DG method can be characterized as the fusion of finite elements with finite volumes. This DG formulation uses high-order Lagrange polynomials on the triangle using nodal sets up to 15th order. Both the area and boundary integrals are evaluated using order $2N$ Gauss cubature rules. The use of exact integration for the area integrals leads naturally to a full mass matrix; however, by using straight-edged triangles we eliminate the mass matrix completely from the discrete equations. Besides obviating the need for a mass matrix, triangular elements offer other obvious advantages in the construction of oceanic shallow water models, specifically the ability to use unstructured grids in order to better represent the continental coastlines for use in tsunami modeling. In this paper, we focus primarily on testing the discrete spatial operators by using six test cases—three of which have analytic solutions. The three tests having analytic solutions show that the high-order triangular DG method exhibits exponential convergence. Furthermore, comparisons with a spectral element model show that the DG model is superior for all polynomial orders and test cases considered. Copyright © 2007 John Wiley & Sons, Ltd.

Received 9 October 2006; Revised 11 May 2007; Accepted 27 May 2007

KEY WORDS: Fekete; finite element; finite volume; Lagrange; penalty method; spectral element

1. INTRODUCTION

The discontinuous Galerkin (DG) method has come into prominence in the last decade in all areas of numerical modeling; however, it was only in the last few years that this method has received attention in geophysical fluid dynamics. The high-order accuracy, geometric flexibility to use unstructured grids, local conservation, and monotonicity properties of the DG method make it

*Correspondence to: F. X. Giraldo, Department of Applied Mathematics, Naval Postgraduate School, Monterey, CA 93943, U.S.A.
†E-mail: fxgirald@nps.edu

Contract/grant sponsor: Office of Naval Research; contract/grant number: PE-0602435N

a prime candidate for the construction of future ocean and shallow water models. The advantages offered by the DG method will benefit all areas of ocean modeling but, specifically, it will improve coastal ocean models where proper coastline representation, and the ability to handle steep gradients (such as tidal bores) will translate into better modeling of tsunamis, storm surges, and hurricanes. Mature tsunami models are already in existence [1, 2] but these models are based on low-order finite difference and finite element methods; below we discuss the advantages of the discontinuous Galerkin method over other spatial discretization methods. The ultimate goal is the development of a nonhydrostatic geometrically flexible coastal ocean model, but in order to achieve this point first requires the development and benchmarking of a shallow water model. Let us now review the literature concerning the application of the DG method to the shallow water equations.

Schwaneberg and Köngeter [3] first used the DG method for the planar shallow water equations, followed by the work of Li and Liu [4], and Aizinger and Dawson [5]. Dupont and Lin [6], Eskilsson and Sherwin [7], Remacle *et al.* [8], and Kubatko *et al.* [9] constructed shallow water models on triangles using a collapsed local coordinate (modal) discontinuous Galerkin method; while all four of these works made extensive use of grid generation to solve their problems, the work of Remacle *et al.* focused primarily on adaptivity with linear polynomials for dam-break problems. Giraldo *et al.* [10] first used the DG method for the shallow water equations on the sphere, which was later followed by the construction of such models on triangular domains (see [11]); however, our work has focused on the nodal space approximations (Lagrange polynomials) rather than the more commonly used modal space approximations (which use Jacobi polynomials). Based on the success of the DG method for these applications, we have now turned our attention to the oceanic shallow water equations where it is expected that this method will have a much greater impact due to its natural ability to handle unstructured triangulations which is necessary in order to resolve coastlines properly.

There are other local high-order methods that have been proposed for ocean and shallow water models, most notably the spectral element (SE) method. This method was first proposed for the oceanic shallow water equations by Ma [12], and later by Iskandarani *et al.* [13]. This method has been applied to the hydrostatic ocean equations [14] and also to the non-hydrostatic equations [15]. There are three reasons to choose DG over the SE method. First, the SE's lack of conservation can adversely affect the accuracy of long time-scale integrations. Secondly, the SE method in its current form can only be used with quadrilateral grids, which are not sufficiently flexible to allow for the automatic construction of detailed grids over general complex coastlines—a goal easily accomplished with triangular grid methods. A caveat is in order here: triangular SE methods have been recently proposed by Giraldo and Taylor [16] but require more analysis before they can be used for such models. The third reason for choosing DG over SE is that, unlike the SE method, the DG method does not require grid staggering of the solution variables to avoid spurious pressure modes encountered in the incompressible limit of the equations.

It should be mentioned that very mature unstructured grid ocean models using the finite element (e.g. see [17, 18]) and finite volume methods (e.g. see [19, 20]) are already in existence; however, the emphasis of our work here is on discontinuous Galerkin models using triangular grids—an approach which, at this point, is still at an early stage of development. The reason for proposing the DG method over the FE method is that the FE method shares some of the same issues as the SE method, that is, grid staggering of the solution variables is required in order to satisfy the Ladyshenskaya–Babuska–Brezzi (LBB) condition and local conservation is lost; however, triangular finite elements are extremely useful for constructing adaptive unstructured grid models. The finite volume method is the low-order cousin of the DG method and therefore shares all of

DOI: 10.1002/fld

the same properties; the only advantage that DG has over FV is that arbitrarily high order can be used.

The remainder of the paper is organized as follows. Section 2 describes the governing equations of motion used to test our numerical method. In Section 3, we describe the spatial discretization of the governing equations and in Section 4 the time integrator used. Finally, in Section 5, we present convergence rates for the triangular DG and quadrilateral SE models. This then leads to some discussion about the performance of the DG model and a summary on the direction of future work.

2. CONTINUOUS EQUATIONS

The oceanic shallow water equations are a system of nonlinear partial differential equations which govern the motion of a viscous incompressible fluid in a shallow depth. The predominant feature of this type of fluid is that the characteristic length of the fluid is far greater than its depth which is analogous to the motion of water in the oceans. For this reason, these equations are typically used as a first step toward the construction of ocean models.

The shallow water equations in conservation form are

$$\frac{\partial \mathbf{q}}{\partial t} + \nabla \cdot \mathbf{F}(\mathbf{q}) = S(\mathbf{q}) \tag{1}$$

where $\mathbf{q} = (\phi, \phi\mathbf{u}^{\mathrm{T}})^{\mathrm{T}}$ are the conservation variables,

$$\mathbf{F}(\mathbf{q}) = \begin{pmatrix} \phi\mathbf{u} \\ \phi\mathbf{u} \otimes \mathbf{u} + \frac{1}{2}\phi^2 \mathscr{I}_2 - \nu\nabla(\phi\mathbf{u}) \end{pmatrix} \tag{2}$$

is the flux tensor and

$$S(\mathbf{q}) = -\begin{pmatrix} 0 \\ f(\mathbf{k} \times \phi\mathbf{u}) + \phi\nabla\phi^s - \dfrac{\boldsymbol{\tau}}{\rho} + \gamma\phi\mathbf{u} \end{pmatrix} \tag{3}$$

is the source function where the nabla operator is defined as $\nabla = (\partial_x, \partial_y)^{\mathrm{T}}$, $\otimes$ denotes the tensor product operator, ϕ is the geopotential height ($\phi = gh$, where g is the gravitational constant and h is the free surface height of the fluid), ϕ^s is the bathymetry (e.g. bottom of the ocean), $\mathbf{u} = (u, v)^{\mathrm{T}}$ is the velocity vector, $f = f_0 + \beta(y - y_m)$ is the Coriolis parameter, $k = (0, 0, 1)^{\mathrm{T}}$ is the unit normal vector of the x–y plane, and the term $\mathscr{I}_2$ is a rank-2 identity matrix. The vector $\boldsymbol{\tau}$ is the wind stress, and the constant γ is the bottom friction. In Equations (1)–(3), we write the complete oceanic shallow water equations but in the current study we exclude bathymetry and viscosity—these are reserved for future studies.

2.1. Linearized continuous equations

Since we do not have analytic solutions to the nonlinear equations, we then use the linearized equations to be able to discern the accuracy of our DG model. To derive this linearized form of

DOI: 10.1002/fld

the equations, we begin by introducing the following expansion of the solution vector in terms of a small perturbation and a mean flow value such that

$$\phi = \phi' + \Phi$$

and

$$\mathbf{u} = \mathbf{u}' + \mathbf{U}$$

Inserting this expansion into Equations (1)–(3) yields

$$\frac{\partial \phi}{\partial t} + \nabla \cdot (\Phi \mathbf{u}) = 0 \tag{4}$$

$$\frac{\partial \Phi \mathbf{u}}{\partial t} + \nabla \cdot (\Phi \phi \mathscr{I}_2) = -f(\mathbf{k} \times \Phi \mathbf{u}) - \gamma \Phi \mathbf{u} + \frac{\boldsymbol{\tau}}{\rho} \tag{5}$$

where we have eliminated the viscous and bathymetry terms since they are not used in this paper. In addition, the primes have been dropped from the equations but it should be understood that the lower case variables are in fact perturbations from the mean flow. Note that the derivation of the linear equations presented assumes that there is no mean flow velocity.

The maximum eigenvalue of the nonlinear flux tensor $\mathbf{F}$ given in Equation (1) is $\lambda_{NL} = u_N + \sqrt{\phi}$, where $u_N = \mathbf{N} \cdot \mathbf{u}$ is the component of the velocity normal to the element edge. However, the maximum eigenvalue of the linear flux tensor given in Equation (5) is $\lambda_L = \sqrt{\Phi}$; these λs are the wave speeds of the system which are used in the Rusanov flux for computing the numerical fluxes and are described in Section 3.4.

3. TRIANGULAR DISCONTINUOUS GALERKIN METHOD

In this section, we describe the discretization of the shallow water equations by the discontinuous Galerkin method on triangles. This includes the choice of basis functions, integration, construction of the semi-discrete problem, and its corresponding matrix form which then allows us to eliminate the mass matrix.

3.1. Basis functions

To define the discrete local operators, we begin by decomposing the domain Ω into N_e conforming non-overlapping triangular elements Ω_e such that

$$\Omega = \bigcup_{e=1}^{N_e} \Omega_e$$

The condition on grid conformity, however, is not required by the DG method; we only impose this condition to simplify the exposition.

To perform differentiation and integration operations, we introduce the nonsingular mapping $\mathbf{x} = \Psi(\boldsymbol{\xi})$ which defines a transformation from the physical Cartesian coordinate system $\mathbf{x} = (x, y)^{\mathrm{T}}$ to the local reference coordinate system $\boldsymbol{\xi} = (\xi, \eta)^{\mathrm{T}}$ defined on the reference triangle $\Omega_e = \{(\xi, \eta), -1 \leqslant \xi, \eta \leqslant 1, \xi + \eta \leqslant 0\}$.

DOI: 10.1002/fld

Let us now represent the local elementwise solution $\mathbf{q}$ by an Nth order polynomial in $\boldsymbol{\xi}$ as

$$\mathbf{q}_N(\boldsymbol{\xi}) = \sum_{i=1}^{M_N} \psi_i(\boldsymbol{\xi}) \mathbf{q}_N(\boldsymbol{\xi}_i) \tag{6}$$

where $\boldsymbol{\xi}_i$ represents $M_N = \frac{1}{2}(N+1)(N+2)$ interpolation points and $\psi_i(\boldsymbol{\xi})$ are the associated multivariate Lagrange polynomials. For the interpolation points $\boldsymbol{\xi}_i$, we choose the nodal sets based on the electrostatics [21] and Fekete [22] points; for simplicity, we shall refer to this nodal set as Fekete points. Let us now describe the construction of the nodal basis functions using the Proriol–Koornwinder–Dubiner (PKD) polynomials [23–25].

We construct the Lagrange polynomials (nodal basis functions), $\psi_k(\xi, \eta)$, on the reference triangle which are implicitly defined by their cardinal nature, by reference to an easily constructed orthonormal PKD polynomial basis [23–25]. This basis is defined as

$$\varphi_k(\xi, \eta) = \sqrt{\frac{(2i+1)(i+j+1)}{2}} P_i^{0,0}\left(\frac{2\xi+\eta+1}{1-\eta}\right)\left(\frac{1-\eta}{2}\right)^i P_j^{2i+1,0}(\eta) \tag{7}$$

where $P_n^{\alpha,\beta}(\xi)$ represents the nth order Jacobi polynomial in the interval $-1 \leqslant \xi \leqslant 1$, $k = i + j(N+1) + 1$, and the indices vary as $0 \leqslant i, j; i + j \leqslant N$, and $k = 1, \ldots, M_N$.

We next seek an explicit formula for the Lagrange basis by representing them in terms of the reference basis, i.e.

$$\psi_i(\xi, \eta) = \sum_{k=1}^{M_N} A_{ik} \varphi_k(\xi, \eta) \tag{8}$$

where the indices are now defined as $i, j, k = 1, \ldots, M_N$. We then use the cardinal property of the Lagrange polynomials

$$\delta_{ij} = \sum_{k=1}^{M_N} A_{ik} \varphi_k(\xi_j, \eta_j)$$

where δ is the Kronecker delta function, to determine that

$$A_{ik} = (\varphi_k^{-1}(\xi_i, \eta_i))^{\mathrm{T}} \tag{9}$$

Since

$$V_{jk} = \varphi_k(\xi_j, \eta_j) \tag{10}$$

is the generalized Vandermonde matrix and using Equations (8), (9), and (10) we construct the Lagrange polynomials as follows:

$$\psi_i(\xi, \eta) = \sum_{k=1}^{M_N} (V^{-1})_{ik}^{\mathrm{T}} \varphi_k(\xi, \eta) \tag{11}$$

Alternatively, one could use the PKD polynomials themselves as the basis functions as is done in [7, 9] which then yields a modal representation (spectral or amplitude–frequency space) of the solution variables instead of the nodal representation (physical space) that we propose. Both the modal and nodal representations should yield the same accuracy; however, the difference

DOI: 10.1002/fld

between these two forms will be in their relative efficiencies (i.e. computational cost). In the future, comparison studies between these two forms should be performed in order to quantify their performance but for now we shall proceed only with the nodal representation.

3.2. Integration

3.2.1. Area integrals. In order to complete the discussion of the local elementwise operations required to construct discrete spatial operators, we must describe the integration procedure required by the weak formulation of all Galerkin methods. For any two functions f and g, the 2D (area) integration $\mathscr{I}_A$ proceeds as follows:

$$\mathscr{I}_A[f, g] = \int_{\Omega_e} f(\mathbf{x}) g(\mathbf{x})\, d\mathbf{x} = \sum_{i=1}^{M_C} w_i^e |J^e(\boldsymbol{\xi}_i)| f(\boldsymbol{\xi}_i)\, g(\boldsymbol{\xi}_i)$$

where M_C is a function of C which represents the order of the cubature approximation. For w_i and $\boldsymbol{\xi}_i$, we use the high-order cubature rules for the triangle given in [26–29]; because we use order $2N$ integration, which is exact for this equation set, then neither spatial filters nor smoothing diffusion operators are used in any of the DG simulations.

3.2.2. Boundary integrals. The DG method also requires the evaluation of boundary integrals, which is the mechanism by which the fluxes across element edges are evaluated and allows the discontinuous elements to communicate. For any two functions f and g, the 1D (boundary) integration $\mathscr{I}_B$ proceeds as follows:

$$\mathscr{I}_B[f, g] = \int_{\Gamma_e} f(\mathbf{x}) g(\mathbf{x})\, d\mathbf{x} = \sum_{i=0}^{Q} w_i^s |J^s(\boldsymbol{\xi}_i)| f(\boldsymbol{\xi}_i) g(\boldsymbol{\xi}_i)$$

where Q represents the order of the quadrature approximation. Using the Gauss quadrature, we can use $Q = N$ to achieve order $2N$ accuracy.

3.3. Tangent and normal vectors of the element edges

In the following, it will become evident that in order to construct a discontinuous Galerkin discretization requires knowledge about the element geometry. In continuous Galerkin methods such as finite and SE methods the only required information is the basis functions, metric terms, and cubature rules. The DG method requires all of this finite element-type information plus some finite volume-type information regarding the element edges and the element neighbors sharing these edges. However, the good news for the DG method is that regardless of the order of the basis function, N, each element only has three edge neighbors (this is true only for conforming grids). This is the process by which a DG element shares its local information with its neighbors.

In Figure 1, we show a schematic of a master element along with its three normal vectors. Note that the tangent vectors for the three edges are given as $\mathbf{t}^1 = \partial\mathbf{x}/\partial\xi$, $\mathbf{t}^2 = -\partial\mathbf{x}/\partial\xi + \partial\mathbf{x}/\partial\eta$, and $\mathbf{t}^3 = -\partial\mathbf{x}/\partial\eta$. The normal vectors are computed by taking the cross product of the tangent vectors with the unit vector in the z direction (i.e. $\mathbf{k} = (0, 0, 1)^{\mathrm{T}}$) which yields $\mathbf{n}^s = t_y^s\mathbf{i} - t_x^s\mathbf{j}$ where $\mathbf{t}^s = t_x^s\mathbf{i} + t_y^s\mathbf{j}$ is the tangent vector and the superscript s denotes the sides/edges ($s = 1, \ldots, 3$). Note that because we are using straight-edged triangles we only have one normal vector per edge.

DOI: 10.1002/fld

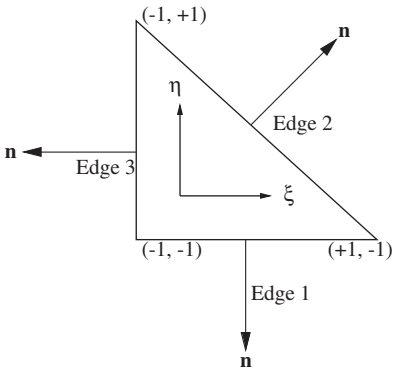

Figure 1. The normal vectors of the master triangle.

3.4. Semi-discrete equations

Applying the discontinuous Galerkin discretization to Equation (1), and using Green's theorem yields the classical DG which we refer to as the *weak* form

$$\int_{\Omega_e} \left(\frac{\partial \mathbf{q}_N}{\partial t} - \mathbf{F}_N \cdot \nabla - S_N \right) \psi_i(\mathbf{x}) \, d\mathbf{x} = - \int_{\Gamma_e} \psi_i(\mathbf{x}) \mathbf{n} \cdot \mathbf{F}_N^* \, d\mathbf{x} \tag{12}$$

where $F_N = F(\mathbf{q}_N)$ and $S_N = S(\mathbf{q}_N)$ with $\mathbf{F}$ and S given by Equations (2) and (3), respectively. Note that Equation (12) states that $\mathbf{q}_N$ satisfies the equation on each element Ω_e for all $\psi \in \mathscr{S}$ where $\mathscr{S}$ is the finite-dimensional space

$$\mathscr{S} = \{ \psi \in \mathscr{L}_2(\Omega) : \psi|_{\Omega_e} \in P_N(\Omega_e) \ \forall \Omega_e \}$$

P_N is the polynomial space defined on Ω_e and the union of these elements defines the entire global domain—that is, $\Omega = \bigcup_{e=1}^{N_e} \Omega_e$ with N_e representing the total number of triangular elements. It should be mentioned that in DG methods, the space $P_N - P_N$ is used without having to worry about violating the inf–sup (LBB) condition which must be observed by continuous Galerkin methods (such as the SE method) in order to avoid the effects of spurious pressure modes. In the boundary integral of Equation (12) $\mathbf{n}$ is the outward pointing unit normal vector of the element edge Γ_e and $\mathbf{F}_N^*$ is the Rusanov numerical flux

$$\mathbf{F}_N^* = \tfrac{1}{2}[\mathbf{F}_N(\mathbf{q}_N^{\mathrm{L}}) + \mathbf{F}_N(\mathbf{q}_N^{\mathrm{R}}) - |\lambda|(\mathbf{q}_N^{\mathrm{R}} - \mathbf{q}_N^{\mathrm{L}})\mathbf{n}] \tag{13}$$

where $\lambda = \max(|U^{\mathrm{L}}| + \sqrt{\phi^{\mathrm{L}}}, |U^{\mathrm{R}}| + \sqrt{\phi^{\mathrm{R}}})$ with $U^{\mathrm{L,R}} = \mathbf{u}^{\mathrm{L,R}} \cdot \mathbf{n}$ being the normal component of velocity with respect to the edge Γ_e, and the superscripts L and R represent the left and right sides of the element edge. The normal vector $\mathbf{n}$ is defined as pointing outward from left to right.

Integrating Equation (12) by parts once again yields the *strong* form

$$\int_{\Omega_e} \psi_i(\mathbf{x}) \left(\frac{\partial \mathbf{q}_N}{\partial t} + \nabla \cdot \mathbf{F}_N - S_N \right) d\mathbf{x} = \int_{\Gamma_e} \psi_i(\mathbf{x}) \mathbf{n} \cdot (\mathbf{F}_N - \mathbf{F}_N^*) \, d\mathbf{x} \tag{14}$$

which, although mathematically equivalent to the weak form, yields different numerical solutions. Based on previous studies (see [11, 30]), we use the strong form exclusively in this paper.

DOI: 10.1002/fld

3.5. Matrix form of the semi-discrete equations

Using the polynomial approximation

$$\mathbf{q}_N = \sum_{i=1}^{M_N} \psi_i \mathbf{q}_i$$

we can now write the semi-discrete system as

$$\int_{\Omega_e} \psi_i \psi_j \, \mathrm{d}\mathbf{x} \frac{\partial \mathbf{q}_j}{\partial t} + \int_{\Omega_e} \psi_i \nabla \psi_j \, \mathrm{d}\mathbf{x} \cdot \mathbf{F}_j - \int_{\Omega_e} \psi_i \psi_j \, \mathrm{d}\mathbf{x} S_j = \int_{\Gamma_e} \psi_i \psi_j \mathbf{n} \, \mathrm{d}\mathbf{x} \cdot (\mathbf{F} - \mathbf{F}^*)_j \tag{15}$$

Next, note that by defining the following elemental matrices

$$M_{ij}^e = \int_{\Omega_e} \psi_i \psi_j \, \mathrm{d}\mathbf{x}, \quad \mathbf{M}_{ij}^s = \int_{\Gamma_e} \psi_i \psi_j \mathbf{n} \, \mathrm{d}\mathbf{x}, \quad \mathbf{D}_{ij}^e = \int_{\Omega_e} \psi_i \nabla \psi_j \, \mathrm{d}\mathbf{x}$$

allows us to write Equation (15) in the following matrix form:

$$M_{ij}^e \frac{\partial \mathbf{q}_j^e}{\partial t} + (\mathbf{D}_{ij}^e)^{\mathrm{T}} \mathbf{F}_j^e - M_{ij}^e S_j = (\mathbf{M}_{ij}^s)^{\mathrm{T}} (\mathbf{F} - \mathbf{F}^*)_j^e \tag{16}$$

where the superscript e denotes an element-based evaluation and the s denotes side-based (or edge-based) evaluation. At this stage we have a mass matrix, M, to contend with since we are using exact integration. Note that since the SE method uses inexact integration then this mass matrix, although global, is diagonal.

Now, let us evaluate the elemental matrices not in terms of the physical variables ($\mathbf{x}$) but in terms of the computational variables ($\boldsymbol{\xi}$). Thus, we can now write

$$M_{ij}^e = |J^e| \int_{\widehat{\Omega}_e} \psi_i \psi_j \, \mathrm{d}\boldsymbol{\xi} \equiv |J^e| M_{ij}$$

$$\mathbf{D}_{ij}^e = |J^e| \int_{\widehat{\Omega}_e} \psi_i \nabla_{\boldsymbol{\xi}} \psi_j \frac{\partial \boldsymbol{\xi}}{\partial \mathbf{x}} \, \mathrm{d}\boldsymbol{\xi} \equiv |J^e| (D_{ij}^{\xi} \xi_x^e + D_{ij}^{\eta} \eta_x^e)\mathbf{i} + |J^e| (D_{ij}^{\xi} \xi_y^e + D_{ij}^{\eta} \eta_y^e)\mathbf{j}$$

$$\mathbf{M}_{ij}^s = |J^s| \int_{\widehat{\Gamma}_e} \psi_i \psi_j \mathbf{n} \, \mathrm{d}\boldsymbol{\xi} \equiv |J^s| M_{ij}^s (n_x^s \mathbf{i} + n_y^s \mathbf{j})$$

where all of the metric terms have been factored from the integrals because for straight-edged triangles they are constant for each element and are defined as $|J^e| = 2\Delta^e$ and $|J^s| = 2\Delta^s$, where Δ^e and Δ^s denote the area of element e and the length of edge s. Furthermore, in these integrals, the gradient operator $\nabla_{\boldsymbol{\xi}}$ is defined in the local reference coordinate system $\boldsymbol{\xi}$, and $\widehat{\Omega}_e$ and $\widehat{\Gamma}_e$ denote the area and boundary domains in the computational space—that is, the bounds of integration for the master element. We can now rewrite Equation (16) in the following way:

$$\begin{aligned} &|J^e| M_{ij} \frac{\partial \mathbf{q}_j^e}{\partial t} + |J^e| (D_{ij}^{\xi} \xi_x^e + D_{ij}^{\eta} \eta_x^e) \mathbf{f}_j^e + |J^e| (D_{ij}^{\xi} \xi_y^e + D_{ij}^{\eta} \eta_y^e) \mathbf{g}_j^e - |J^e| M_{ij} S_j^e \\ &\quad = |J^s| M_{ij}^s [n_x^s (\mathbf{f}^e - \mathbf{f}^*)_j + n_y^s (\mathbf{g}^e - \mathbf{g}^*)_j] \end{aligned} \tag{17}$$

where $\mathbf{F}^e = \mathbf{f}^e \mathbf{i} + \mathbf{g}^e \mathbf{j}$.

DOI: 10.1002/fld

3.5.1. Elimination of the mass matrix. Let us see how we can eliminate the mass matrix from Equation (17). Taking Equation (17) and dividing by $|J^e|$ and left multiplying by M_{ij}^{-1}, we get

$$\frac{\partial \mathbf{q}_i^e}{\partial t} + (\widehat{D}_{ij}^{\xi}\xi_x^e + \widehat{D}_{ij}^{\eta}\eta_x^e)\mathbf{f}_j^e + (\widehat{D}_{ij}^{\xi}\xi_y^e + \widehat{D}_{ij}^{\eta}\eta_y^e)\mathbf{g}_j^e - S_i^e = \frac{|J^s|}{|J^e|}\widehat{M}_{ij}^s[n_x^s(\mathbf{f}^e - \mathbf{f}^*)_j + n_y^s(\mathbf{g}^e - \mathbf{g}^*)_j] \tag{18}$$

where the matrices are defined as

$$\widehat{D}_{ij}^{\xi} = M_{ik}^{-1}D_{kj}^{\xi}, \quad \widehat{D}_{ij}^{\eta} = M_{ik}^{-1}D_{kj}^{\eta}, \quad \widehat{M}_{ij}^s = M_{ik}^{-1}M_{kj}^s \tag{19}$$

where

$$M_{ij} = \sum_{k=1}^{M_C} w_k\psi_{ik}\psi_{jk}, \quad M_{ij}^s = \sum_{k=1}^{M_Q} w_k\psi_{ik}\psi_{jk} \tag{20}$$

$$D_{ij}^{\xi} = \sum_{k=1}^{M_C} w_k\psi_{ik}\frac{\partial\psi_{jk}}{\partial\xi}, \quad D_{ij}^{\eta} = \sum_{k=1}^{M_C} w_k\psi_{ik}\frac{\partial\psi_{jk}}{\partial\eta} \tag{21}$$

and M_C and M_Q denote the number of cubature (two dimensional) and quadrature (one dimensional) integration points required to achieve order $2N$ accuracy, and ψ_{ik} represents the function ψ at the $i = 1, \ldots, M_N$ interpolation points evaluated at the integration point k.

Observing the hat matrices in Equation (19), it is not at all obvious that we have eliminated the mass matrix from the equations; instead it just looks as if we have premultiplied all the terms by the mass matrix. This is only partly true. Since the mass matrix is constant (i.e. not a function of $\mathbf{x}$) then, using Equations (20) and (21), we can move the mass matrix inside the summations which are the discrete representations of the continuous integrals. This then gives

$$\widehat{M}_{ij}^s = \sum_{k=1}^{M_Q} w_k\widehat{\psi}_{ik}\psi_{jk}, \quad \widehat{D}_{ij}^{\xi} = \sum_{k=1}^{M_C} w_k\widehat{\psi}_{ik}\frac{\partial\psi_{jk}}{\partial\xi}, \quad \widehat{D}_{ij}^{\eta} = \sum_{k=1}^{M_C} w_k\widehat{\psi}_{ik}\frac{\partial\psi_{jk}}{\partial\eta}$$

where

$$\widehat{\psi}_i = M_{ik}^{-1}\psi_k$$

is the basis function premultiplied by the inverse mass matrix. Absorbing the mass matrix within the test function $\widehat{\psi}$ completely eliminates the mass matrix from Equation (18) without making any approximations—that is, we are guaranteed to get the same accuracy as if we had chosen not to eliminate the mass matrix. The elimination of the mass matrix can only be accomplished, when using Lagrange polynomials in nodal space, if and only if straight-edged triangles are used. Note that for the PKD polynomials (modal space DG), the mass matrix is diagonal only for straight-edged triangles. We have chosen the nodal space primarily because we want to avoid the transformations from modal to nodal space when implementing physical boundary conditions required by coastal models near open boundaries (i.e. when conditions from a global ocean model are required as the forcing for the coastal oceanic shallow water model).

DOI: 10.1002/fld

3.6. Slope limiter

While the thrust of the current work is not in the construction of monotone solutions, for the Riemann problem considered in Section 5, a slope limiter is required in order to avoid spurious oscillations in the vicinity of the discontinuity. For this purpose, we now describe a simple slope limiter based on the spectral filter for nodal triangular-based SEs described in Giraldo and Warburton [31].

Using the definition of the Vandermonde matrix given in Equation (10), we can expand the solution vector $\mathbf{q}$ using the modal PKD polynomial space as

$$\mathbf{q}_i = V_{ij}\widetilde{\mathbf{q}}_j \tag{22}$$

where V is the Vandermonde matrix, $\widetilde{\mathbf{q}}$ are the modal (spectral) space expansion coefficients, and $i, j = 1, \ldots, M_N$. Left multiplying Equation (22) by the inverse Vandermonde matrix yields

$$\widetilde{\mathbf{q}}_i = V_{ij}^{-1}\mathbf{q}_j \tag{23}$$

In the modal (amplitude–frequency) space, we now know which mode represents the constant amplitude wave and which modes represent the amplitudes of the high-order frequency waves. Thus, to enforce monotonicity without destroying local conservation, we adjust the high-frequency modes without changing the constant mode. This is the general idea behind slope limiting; however, for the purposes of this paper we only focus on the construction of a limiter for linear polynomials. That is, all we have to do is to eliminate the linear modes while retaining the constant mode; let us represent this operation by the diagonal matrix Λ. Upon applying this limiter, we are left with the new modal coefficients $\widetilde{\mathbf{q}}^{\mathrm{L}}$ where the superscript L refers to the limited solution. At this point, we then left multiply $\widetilde{\mathbf{q}}^{\mathrm{L}}$ by the Vandermonde matrix to obtain the limited nodal (physical) space solution vector $\mathbf{q}^{\mathrm{L}}$. Note that the entire slope limiting operation can be defined by the following matrix–vector multiplication:

$$\widetilde{\mathbf{q}}_i^{\mathrm{L}} = \mathscr{M}_{ij}\mathbf{q}_j \tag{24}$$

where

$$\mathscr{M}_{ij} = V_{ik}^{-1}\Lambda_{kl}V_{lj} \tag{25}$$

defines the slope limiting matrix. In order to determine when to apply the limiter defined in Equation (24), we use the Krivodonova *et al*. discontinuity detector presented in [32].

It should be understood that we do not recommend our slope limiting strategy for general applications. This approach is only useful for linear polynomials; using higher-order polynomials with this approach is wasteful because all the modes except for the constant mode will be eliminated from the solution whenever the limiter is activated by the detector.

3.7. Boundary conditions

In all the test cases, we only consider no-flux boundary conditions. The no-flux boundary conditions are enforced by virtue of the statement

$$\mathbf{n}\cdot\mathbf{u} = 0 \tag{26}$$

at the boundaries. Thus, we seek to eliminate the normal component of the velocity to the no-flux boundary without altering the tangential component (for free slip boundary conditions). The

DOI: 10.1002/fld

tangent vector to a boundary is obtained by $\mathbf{t}=\mathbf{k}\times\mathbf{n}$ which is equal to $\mathbf{t}=-n_y\mathbf{i}+n_x\mathbf{j}$. Thus, we solve the following 2×2 system:

$$\begin{pmatrix} n_x & n_y \\ -n_y & n_x \end{pmatrix}\begin{pmatrix} u \\ v \end{pmatrix}=\begin{pmatrix} 0 \\ u_{\mathrm{T}} \end{pmatrix} \tag{27}$$

where $u_{\mathrm{T}}=\mathbf{t}\cdot\mathbf{u}$ is the tangential component of velocity. This boundary condition is imposed only weakly through the boundary integral in Equation (18); that is, it only comes in through the Rusanov flux.

4. TIME INTEGRATOR

In order to advance the solution in time while retaining some high-order accuracy, we use the strongly stability preserving (SSP) Runge–Kutta third-order (RK3) method of Cockburn and Shu [33]. For completeness we define it now. Let us write the semi-discrete (in space) equations as follows:

$$\frac{\partial\mathbf{q}}{\partial t}=S(\mathbf{q})$$

The SSP temporal discretization of this vector equation is

$$\begin{aligned} &\text{for } k=1,\ldots,3 \\ &\quad \mathbf{q}^k=\alpha_0^k\mathbf{q}^n+\alpha_1^k\mathbf{q}^{k-1}+\beta^k\Delta t\,S(\mathbf{q}^{k-1}) \end{aligned}$$

where $\mathbf{q}^0=\mathbf{q}^n$, $\mathbf{q}^3=\mathbf{q}^{n+1}$ and the coefficients α and β are given in Table I.

5. NUMERICAL EXPERIMENTS

For the numerical experiments, we use the normalized L_2

$$\|h\|_{L_2}=\sqrt{\frac{\int_\Omega (h_{\mathrm{exact}}-h)^2\,\mathrm{d}\Omega}{\int_\Omega h_{\mathrm{exact}}^2\,\mathrm{d}\Omega}}$$

Table I. Coefficients for the strongly stability preserving third-order Runge–Kutta method.

	$k=1$	$k=2$	$k=3$
α_0	1	3/4	1/3
α_1	0	1/4	2/3
β	1	1/4	2/3

DOI: 10.1002/fld

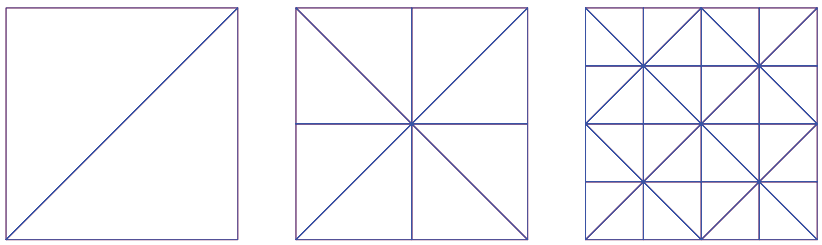

Figure 2. Grid refinement for the structured triangular grids with (a) $n_r = 1$, (b) $n_r = 2$, and (c) $n_r = 4$.

and L_∞

$$\|h\|_{L_\infty} = \frac{\max_{\mathbf{x}\in\Omega} |h|}{\max_{\mathbf{x}\in\Omega} |h_{\text{exact}}|}$$

error norms to judge the accuracy of the models; the error norms are computed at the cubature points. To compute the Courant number, the elements are decomposed into their high-order (HO) grid points (which are in fact the Fekete points) and these grid points form a fine grid which we refer to as the HO cells. The velocities and grid spacings are then defined at the centers of these cells. Using these definitions, the Courant number is then defined as

$$\text{Courant number} = \max \left(\frac{C\Delta t}{\Delta s} \right)_{\text{HO}}^{e} \qquad \forall e \in [1, \ldots, N_e]$$

where $C = U + \sqrt{\phi}$ is the characteristic speed, $U = \sqrt{\mathbf{u} \cdot \mathbf{u}}$ is the magnitude of the velocity, and $\Delta s = \sqrt{\Delta x^2 + \Delta y^2}$ is the grid spacing. For all the results presented, the Courant number is taken to be $\leqslant 0.5$.

For the purpose of studying the convergence properties of the method, we employ hp-refinement. H-refinement refers to when the triangular grids are refined while the order of the polynomial, N, is held constant. In contrast, p-refinement refers to when the order of the polynomial, N, is increased within each element while the total number of triangles is kept constant. To refer to h-refinement, we shall use the symbol n_r which represents a grid refinement level. This variable n_r represents the number of quadrilateral subdivisions in each of the Cartesian directions. For example, $n_r = 1$ corresponds to n_r^2 quadrilaterals and $2n_r^2$ triangles; the factor of 2 is required since each quadrilateral is subdivided into two triangles. Examples of square domains with $n_r = 1$, $n_r = 2$, and $n_r = 4$ are shown in Figure 2.

5.1. Description of the test cases

We now describe the test cases and their solutions. It should be noted that all the tests presented below require no-flux boundary conditions at all four walls. In fact, these are the only boundary conditions that we consider in this work.

5.1.1. Linear standing wave. This problem involves the transient solution of a linear inviscid standing wave without rotation which *sloshes* within a square basin of unit depth. From [13], we

DOI: 10.1002/fld

take the analytic solution as

$$h(\mathbf{x}, t) = \cos \pi x \cos \pi y \cos \sqrt{2}\pi t$$

$$u(\mathbf{x}, t) = \tfrac{1}{\sqrt{2}} \sin \pi x \cos \pi y \sin \sqrt{2}\pi t$$

$$v(\mathbf{x}, t) = \tfrac{1}{\sqrt{2}} \cos \pi x \sin \pi y \sin \sqrt{2}\pi t$$

with $(x, y) \in [0, 1]^2$ and $t \in [0, 2]$. For this problem, the source function, S, in Equation (1) is zero and the flux tensor is linearized.

5.1.2. Linear Kelvin wave. This problem involves the transient solution of the linearized inviscid equations with rotation. From [7], we use the analytic solution

$$h(\mathbf{x}, t) = 1 + \exp\left(-\frac{y^2}{2}\right) \exp\left(-\frac{(x + 5 - t)^2}{2}\right)$$

$$u(\mathbf{x}, t) = \exp\left(-\frac{y^2}{2}\right) \exp\left(-\frac{(x + 5 - t)^2}{2}\right)$$

$$v(\mathbf{x}, t) = 0$$

with $f_0 = 0$, $\beta = 1$, and $(x, y) \in [-10, 10] \times [-5, 5]$ and $t \in [0, 5]$.

5.1.3. Linear Stommel problem. The linear Stommel problem [34] is the exact steady-state solution of the linearized inviscid equations with rotation, wind stress, and bottom friction. From Hanert (personal communication), the steady-state solution to this problem is

$$h(x, y, t \to \infty) = h_{\text{scale}} \mathscr{H}$$

$$u(x, y, t \to \infty) = u_{\text{scale}} \mathscr{U}$$

$$v(x, y, t \to \infty) = u_{\text{scale}} \mathscr{V}$$

where

$$\mathscr{H} = -\frac{R_2}{\pi f_0} \gamma \sin \pi \tilde{y} + \frac{R_1}{\pi} \left(\cos \pi \tilde{y} (1 + \beta_p \tilde{y}) - \frac{\beta_p}{\pi} \sin \pi \tilde{y} \right)$$

$$\mathscr{U} = R_1 \sin \pi \tilde{y}$$

$$\mathscr{V} = R_2 \cos \pi \tilde{y}$$

DOI: 10.1002/fld

is the non-dimensional solution and

$$u_{\text{scale}} = \frac{\tau D}{\rho H \gamma \pi}$$

$$h_{\text{scale}} = \frac{f_0 L u_{\text{scale}}}{g}$$

are the scaling factors. The remainder of the variables are defined as follows:

$$R_1 = \frac{\pi}{D}[1 + ((\mathrm{e}^{R_-} - 1)\mathrm{e}^{R_+\tilde{x}} + (1 - \mathrm{e}^{R_+})\mathrm{e}^{R_-\tilde{x}})/(\mathrm{e}^{R_+} - \mathrm{e}^{R_-})]$$

$$R_2 = \frac{1}{D}(R_+(\mathrm{e}^{R_-} - 1)\mathrm{e}^{R_+\tilde{x}} + R_-(1 - \mathrm{e}^{R_+})\mathrm{e}^{R_-\tilde{x}})/(\mathrm{e}^{R_+} - \mathrm{e}^{R_-})$$

with

$$D = \frac{R_+(\mathrm{e}^{R_-} - 1) + R_-(1 - \mathrm{e}^{R_+})}{\mathrm{e}^{R_+} - \mathrm{e}^{R_-}}$$

$R_\pm = (-1 \pm \sqrt{1 + (2\pi\varepsilon)^2})/2\varepsilon$, and $\varepsilon = \gamma/L\beta$. The remaining constants are defined as $f_0 = 1 \times 10^{-4}$, $\beta = 1 \times 10^{-11}$, $\beta_p = \beta L/f_0$, $\gamma = 1 \times 10^{-6}$, $g = 10$, $\rho = 1000$, $\tau = 0.2$, $H = 1000$, and $L = 1 \times 10^6$. Note that the dimensionless coordinates are defined as $\tilde{\mathbf{x}} = \mathbf{x}/L$, where $(x, y) \in [0, 1000]^2$ km and the equations are integrated between 200 and 800 days in order to reach steady state. For the high-order polynomials (and finer grids), it takes longer to ensure that steady state is reached. We regard steady state as the condition where the error norms cease to decrease.

The analytic solution to this problem accumulates the free surface along the western boundary of the basin. This solution is in fact symmetric with respect to the axis $y = L/2$.

5.1.4. Nonlinear Stommel problem. This case is similar to the linear Stommel problem except that we now use the full equations. The initial and boundary conditions remain the same as in the linear problem. Steady state for the nonlinear Stommel problem is reached between 100 and 200 days.

In the nonlinear problem, the magnitude of the advection terms along the western boundary is quite large which then does not allow the wind stress and the rotation to turn the flow around the top-left corner of the basin. For this reason, unlike in the linear problem, the nonlinear problem accumulates fluid along the top-left corner of the basin. However, the extrema of the free surface height of the linear and nonlinear problems remain similar.

5.1.5. Nonlinear Rossby soliton wave. This problem describes an equatorially trapped Rossby soliton wave [35]. The soliton wave starts off in the center of the domain. It then moves westward along the equator without changing shape. The asymptotically derived analytic solution is given by

$$h(x, y, t) = h^{(0)} + h^{(1)}$$

$$u(x, y, t) = u^{(0)} + u^{(1)}$$

$$v(x, y, t) = v^{(0)} + v^{(1)}$$

DOI: 10.1002/fld

where the superscripts (0) and (1) denote the zeroth- and first-order asymptotic solutions of the shallow water equations, respectively. They are given by

$$h^{(0)} = \eta\left(\frac{-9+6y^2}{4}\right)\mathrm{e}^{-y^2/2}$$

$$u^{(0)} = \frac{\partial\eta}{\partial\xi}(2y)\mathrm{e}^{-y^2/2}$$

$$v^{(0)} = \eta\left(\frac{3+6y^2}{4}\right)\mathrm{e}^{-y^2/2}$$

and

$$h^{(1)} = c^{(1)}\eta\tfrac{9}{16}(-5+2y^2)\mathrm{e}^{-y^2/2} + \eta^2\Phi^{(1)}(y)$$

$$u^{(1)} = c^{(1)}\eta\tfrac{9}{16}(3+2y^2)\mathrm{e}^{-y^2/2} + \eta^2 U^{(1)}(y)$$

$$v^{(1)} = \frac{\partial\eta}{\partial\xi}\eta V^{(1)}(y)$$

where $\eta(\xi,t) = A\,\mathrm{sech}^2\,B\xi$, $\xi = x - ct$, $A = 0.771B^2$, $B = 0.394$, and $c = c^{(0)} + c^{(1)}$ where $c^{(0)} = -\frac{1}{3}$ and $c^{(1)} = -0.395B^2$. The variable η is the solution to the equation

$$\frac{\partial\eta}{\partial\tau} + \alpha_n\eta\frac{\partial\eta}{\partial\xi} + \beta_n\frac{\partial^3\eta}{\partial\xi^3} = 0$$

which is the famous Korteweg–de Vries equation that yields soliton wave solutions. The shallow water equations can be simplified into this equation using the method of multiple scales presented in [36]. Finally, the remaining terms are given by

$$\begin{pmatrix}\Phi^{(1)}(y)\\ U^{(1)}(y)\\ V^{(1)}(y)\end{pmatrix} = \mathrm{e}^{-y^2/2}\sum_{n=0}^{\infty}\begin{pmatrix}\varphi_n\\ u_n\\ v_n\end{pmatrix}H_n(y)$$

where $H_n(y)$ are the Hermite polynomials and φ_n, u_n, v_n are the Hermite series coefficients given in [35]. The Coriolis parameter is given by $f(y) = y$, where $(x, y) \in [-24, +24] \times [-8, +8]$ $t \in [0, 40]$ and $g = 1$.

We include this analytic solution for completeness but one cannot use this test for determining the spectral (exponential) convergence of a method because the analytic solution is only a first-order approximation. However, this solution can be used to check the phase speed of the soliton wave simulated by the numerical model as well as the general shape of the wave.

5.1.6. Nonlinear Riemann problem. The Riemann problem for the shallow water system is also known as the circular dam-break problem. In fact, this test case has been used by various researchers when showing the merits of their conservative numerical models. We follow the outline of the

DOI: 10.1002/fld

problem presented in Toro [37]. In this case, the source function, S, on the right-hand side of Equation (1) is set to zero; thus, we are only left with a balance between the time rate of change of the conservation variable $\mathbf{q}$ and the divergence of the flux tensor. Following [37], we use

$$h(x, y, 0) = \begin{cases} 2.5 & \text{if } r \leqslant R \\ 0.5 & \text{if } r > R \end{cases}$$

with $\mathbf{u}(x, y, 0) = 0 \ \forall (x, y) \in [-20, 20]^2$ where $r = \sqrt{x^2 + y^2}$, $R = 2.5$, and $t \in [0, 0.4]$. Thus, the cylindrical wave is positioned initially at the origin and moves outward for increasing time t. We chose this specific configuration of the problem because there is a detailed study of this problem in the textbook by Toro which allows us to study this test for various times throughout the integration. While we only show results for $t = 0.4$, our results for all time match those in [37] which were obtained by a high-resolution total variation diminishing finite volume method.

5.2. *Convergence properties of the DG model*

To check the convergence rate of the DG model, we use the linear standing wave test. We define the rate of convergence as follows:

$$\text{rate} = \frac{\log[\text{error}_{n_r+1}/\text{error}_{n_r}]}{\log[n_r/(n_r+1)]}$$

where n_r is the h-refinement of the grid for a particular polynomial order. For each polynomial order N, the rate of convergence is averaged over all grid refinement levels.

Figure 3 shows the h normalized L_2 error of the triangular DG model as a function of grid refinement, n_r, for polynomial orders $N = 1, \ldots, 9$. In this figure, we show the convergence rate achieved for each polynomial order. Note that the maximum convergence rate that should be achieved is on the order $N + 1$. From Figure 3, we see that we either reach this limit or approach it quite closely.

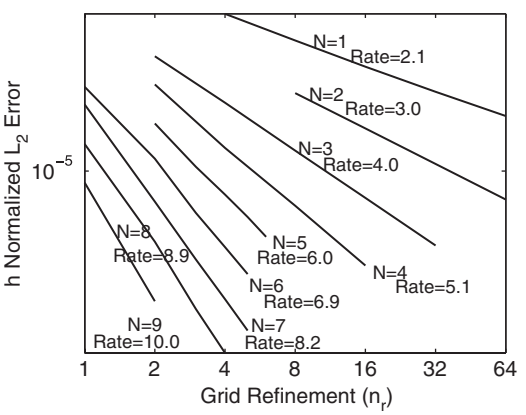

Figure 3. Linear standing wave. The normalized h L_2 error of the DG model as a function of grid refinement, n_r, for the polynomial degrees $N = 1, \ldots, 9$ with their associated convergence rates.

DOI: 10.1002/fld

5.3. Comparison of the DG and SE models

For the purpose of comparing the triangular DG model with another local high-order model, we chose the quadrilateral SE model described in [38] which uses the same numerics as in the well-tested NSEAM global atmospheric model presented in [39]. The model presented in [38] uses the same discretization method as other well-established ocean models such as the one described in [13]. Of particular interest is whether the models achieve exponential (spectral) convergence which is defined as

$$\text{error} \propto \mathcal{O}(\Delta x^{N+1})$$

where Δx is the grid spacing and N is the polynomial order.

Note, however, that we do not give efficiency comparisons between the two models. The main reason for omitting this discussion is because such a discussion is of significant value only when two mature models are compared. At the moment, both the DG and SE models discussed below are in their infancy. At the present time, the SE model is approximately a factor of 2 faster than the DG model; however, the cost of the DG model will not change very much regardless of the type of problems (test cases) studied. In contrast, the SE model presented below does not employ grid staggering which is required in the Stokes limit of viscous problems; grid staggering will reduce the order of accuracy of the SE model while incurring additional computational costs. Other differences between the SE and DG methods that need to be considered are: the additional cost in both memory and efficiency from using the local discontinuous Galerkin (LDG, see [40]) method for viscous problems. On the other hand, SE models require spectral filters to maintain stability which not only degrade the efficiency (especially on distributed-memory computers due to the added communications required), but also the accuracy (see [10, 31]). Therefore, it only makes sense to discuss efficiencies once the models are in a mature state.

5.3.1. Linear standing wave. As was discussed previously, this is an easy test for a numerical model because, although time dependent, the wave undulates smoothly within the basin. Figure 4 shows the h normalized L_2 and L_∞ errors of the free surface height as a function of polynomial order, N, for both the DG and SE models. Both the models use $n_r = 1$ which corresponds to one quadrilateral element for the SE model and two triangular elements for the DG model (see Figure 2(a)). Note that both models yield exponential convergence; however, the triangular high-order DG model yields results almost two orders of magnitude (a factor of 100) more accurate than the SE model. Furthermore, the error curves for the DG model are far smoother than those for the SE model; this indicates the robustness of the DG model for all polynomial orders (odd and even orders yield the expected convergence rate).

5.3.2. Linear Kelvin wave. Figure 5 shows the L_2 and L_∞ error norms of the free surface height as a function of polynomial order, N, for both the DG and SE models. Both models use $n_r^x = 8$ and $n_r^y = 4$ which correspond to 32 quadrilateral elements for the SE model and 64 triangular elements for the DG model. Both models yield exponential convergence; note that for low polynomial orders, the DG model is more accurate than the SE model with the SE model catching up to the DG model near $N = 8$. It is not surprising that the SE model is less accurate than the DG model for $N \leqslant 4$ because for this polynomial order the inexact integration used in SE methods severely affects the accuracy of the method. However, the fact that the SE model only catches up to the

DOI: 10.1002/fld

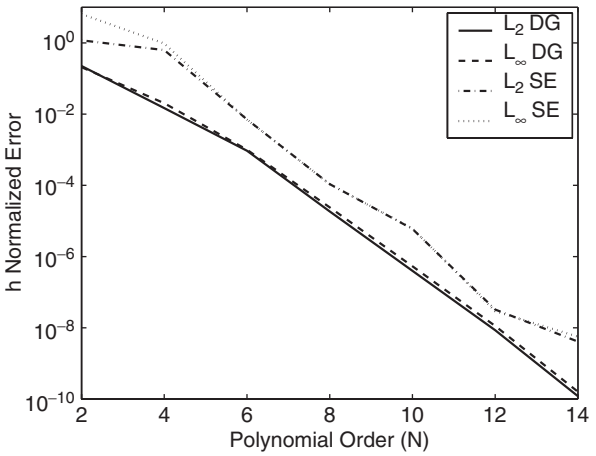

Figure 4. Linear standing wave. The normalized h L_2 and L_∞ errors for the discontinuous Galerkin (DG) and spectral element (SE) models as functions of the polynomial order, N, using $n_r = 1$.

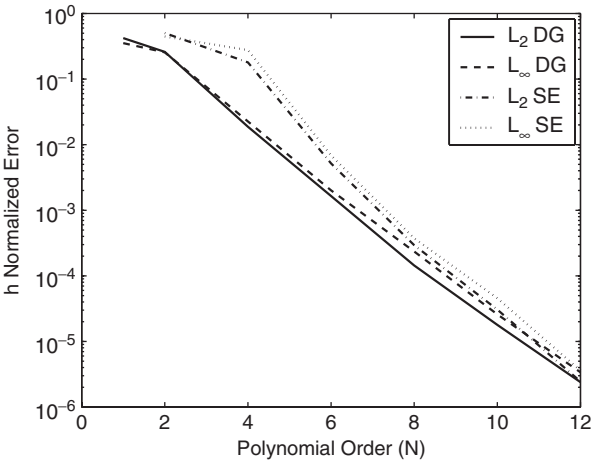

Figure 5. Linear Kelvin wave. The normalized h L_2 and L_∞ errors for the discontinuous Galerkin (DG) and spectral element (SE) models as functions of the polynomial order, N, using $n_r^x = 8$ and $n_r^y = 4$.

DG model near $N = 8$ is a bit surprising. Regardless, the difference in this case is not nearly as significant (less than one order of magnitude) as in the previous test.

5.3.3. Linear Stommel problem. In Figure 6, we show the convergence rates as a function of polynomial order, N, for $n_r = 4$ which corresponds to 16 quadrilateral elements for the SE model and 32 triangular elements for the DG model. Figure 6 shows two important points: the first is that both models yield exponential convergence but the errors for the DG model are much lower than those for the SE model (about two orders of magnitude for $N = 10$). The second point is that the error curves for the DG model are linear and not at all jumpy as for the SE model. This shows

DOI: 10.1002/fld

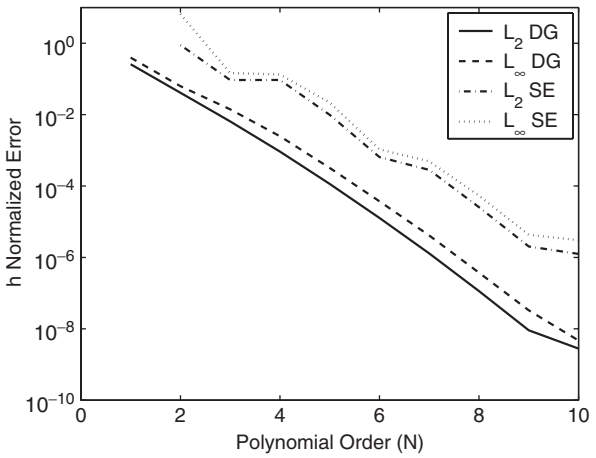

Figure 6. Linear Stommel problem. The normalized h L_2 and L_∞ errors for the discontinuous Galerkin (DG) and spectral element (SE) models as functions of the polynomial order, N, using $n_r = 4$.

that the DG model is more robust in both the odd and even polynomial orders which does not seem to be the case for the SE model.

5.3.4. Nonlinear Stommel problem. Figures 7 and 8 illustrate the grid and the free surface height after 100 days for the nonlinear Stommel problem for both the DG and SE models using $N = 6$ order polynomials. The grids shown include not only the elements (quadrilaterals for the SE model and triangles for the DG model), but also the nodal (interpolation) points. For the purpose of graphics, the interpolation points of the grids are shown to be connected (for the triangles they are connected using their Delaunay triangulations); however, it should be understood that the concept of connectivity of the interior points is irrelevant in both the SE and DG methods. Both grids shown in Figures 7 and 8 are of equal resolution which in this case is $n_r = 10$ and corresponds to 100 quadrilateral elements for the SE model and 200 triangular elements for the DG model. Since we do not have an analytic solution to this problem, we can only compare the results of the two models. From the contour plots, we observe that both models yield the same steady-state solution; that is, the contour levels and their positions are similar.

5.3.5. Nonlinear Rossby soliton wave. As a final comparison test, we run the Rossby soliton wave for 40 time units. Figure 9 shows the solution of the DG and SE models using $N = 8$ order polynomials with a grid refinement of $n_r^x = 24$ and $n_r^y = 8$ which corresponds to 192 quadrilateral elements for the SE model and 384 triangular elements for the DG model. From the plots, both results look approximately the same; compared with the asymptotic solution, we find that both models do indeed approximate the analytic solution quite well. Since the analytic solution is only first order, we cannot claim which model is more accurate. However, the analytic solution predicts that the maximum peak of the wave will be 0.1534 at the position $x = -15.68$. The SE model yields a peak of 0.1478 at $x = -15.36$ while the DG model yields a peak of 0.1484 at $x = -15.56$. Nonetheless, it should be understood that the only information derived from this comparison is that the DG and SE models are behaving similarly for this case.

DOI: 10.1002/fld

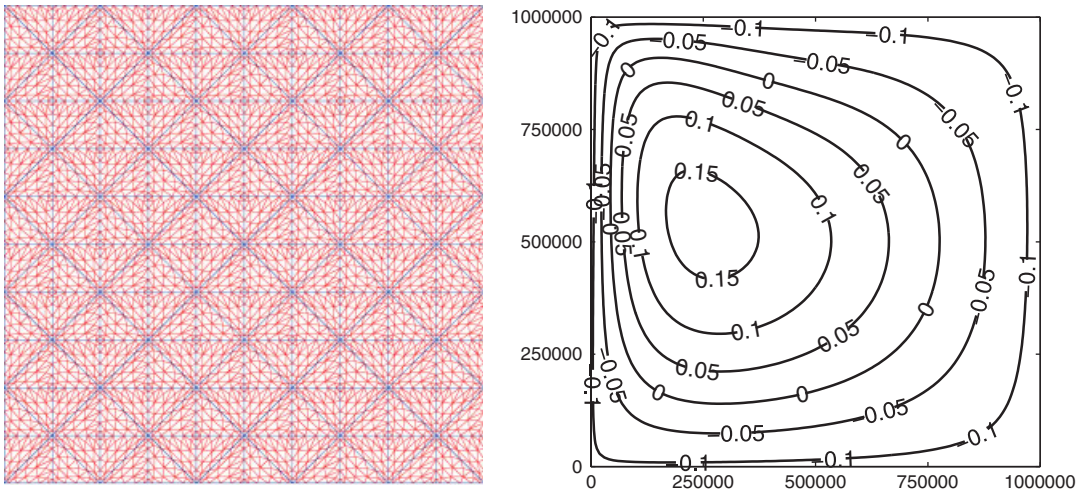

Figure 7. Nonlinear Stommel problem: (a) the grid and (b) the free surface height for $n_r = 10$ and $N = 6$ polynomials for the triangular DG method after 100 days.

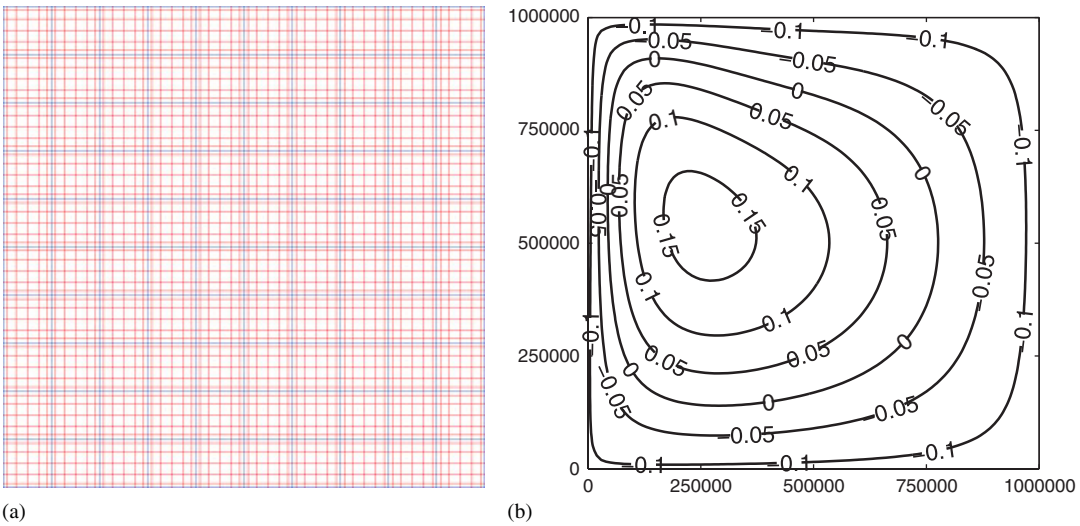

Figure 8. Nonlinear Stommel problem: (a) the grid and (b) the free surface height for $n_r = 10$ and $N = 6$ polynomials for the quadrilateral SE method after 100 days.

5.4. Advantages of unstructured triangulations

One reason for developing discontinuous Galerkin methods on the triangle is to be able to use existing sophisticated grid generators (such as AMATOS described in [41]). While general unstructured quadrilateral grid generators do exist (e.g. CUBIT from Sandia National Laboratory), the triangle (in 2D) is a much more natural choice for adaptive unstructured grid generation

DOI: 10.1002/fld

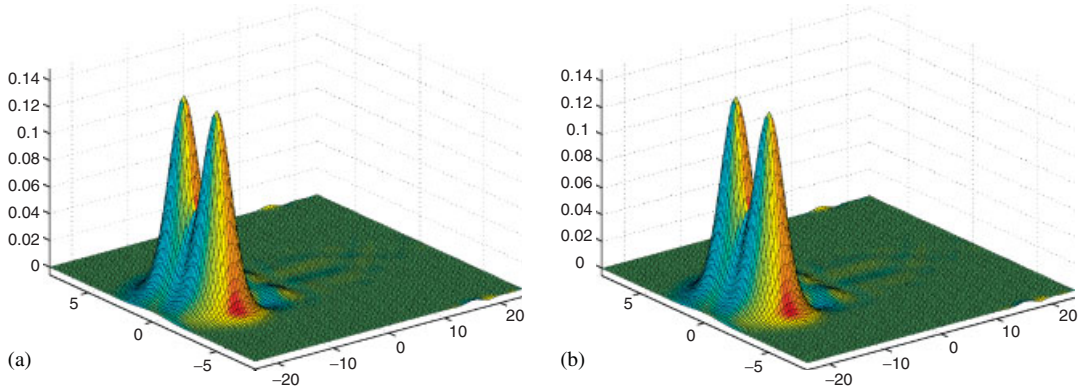

Figure 9. Nonlinear Rossby soliton wave. The free surface height using $N = 8$ polynomials for (a) the discontinuous Galerkin and (b) the spectral element method with $n_r^x = 24$ and $n_r^y = 8$ after 40 time units.

precisely because it is the 2-simplex. To motivate future studies, we now show some advantages of adaptive triangulations.

A few words regarding the grid generator used in this section are in order. This advancing front grid generator takes the solution from a coarse grid and using a scalar variable (in this case the free surface height) constructs an error indicator based on the gradient of the variable. Thus where the magnitude of the gradient vector is large, the mesh is refined and where it is small, the mesh is coarsened. Further information about this adaptive grid generator can be found in [42, 43]. While this particular adaptive grid generator only works for linear elements there are, however, more sophisticated adaptive mesh generators which can handle high-order elements; one example is the AMATOS package developed by Behrens *et al*. [41].

5.4.1. Linear Stommel problem. In Figure 10, we show the grid and free surface height contours for the linear Stommel problem. Figure 10(a) shows the grid and contours for a coarse resolution grid with 206 elements while Figure 10(b) shows the fine resolution grid results with 2984 elements. The L_2 error for these two simulations are 0.0770 and 0.0052, respectively, showing that the error has decreased significantly. Note that the adaptive triangulator has put the majority of elements along the western boundary which is the location of the largest gradients.

5.4.2. Nonlinear Stommel problem. Figure 11 shows the grid and free surface height contours for the nonlinear Stommel problem for the coarse grid (Figure 11(a)) with 206 elements and the fine grid (Figure 11(b)) with 4608 elements. Once again, the adaptive triangulator refined the region near the western boundary of the basin. In fact, due to the nonlinear effects of advection, the gradients are much stronger and for this reason the mesh generator added many more elements than in the linear problem.

5.4.3. Nonlinear Rossby soliton wave. Figure 12 shows the linear grid and free surface height for the nonlinear Rossby soliton wave. Thus, even though both simulations used $N = 8$ polynomials, we only show the vertices of triangular elements (corresponding to $N = 1$), excluding the high-order grid points for clarity. Figure 12(a) shows the results for a structured grid with 260 elements

DOI: 10.1002/fld

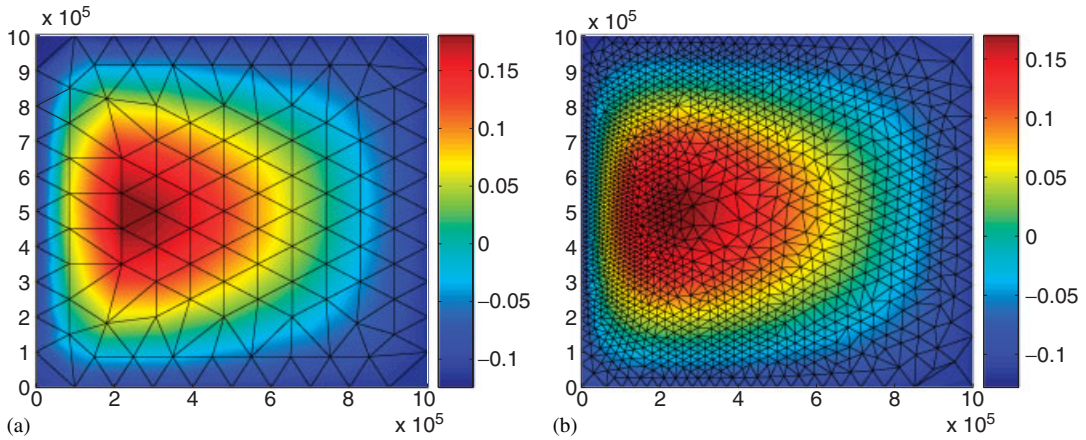

Figure 10. Linear Stommel problem. The grid and color contours of the free surface for (a) an unstructured grid with $N_e = 206$ and (b) an adaptive unstructured grid with $N_e = 2984$ elements, both using $N = 1$ polynomials.

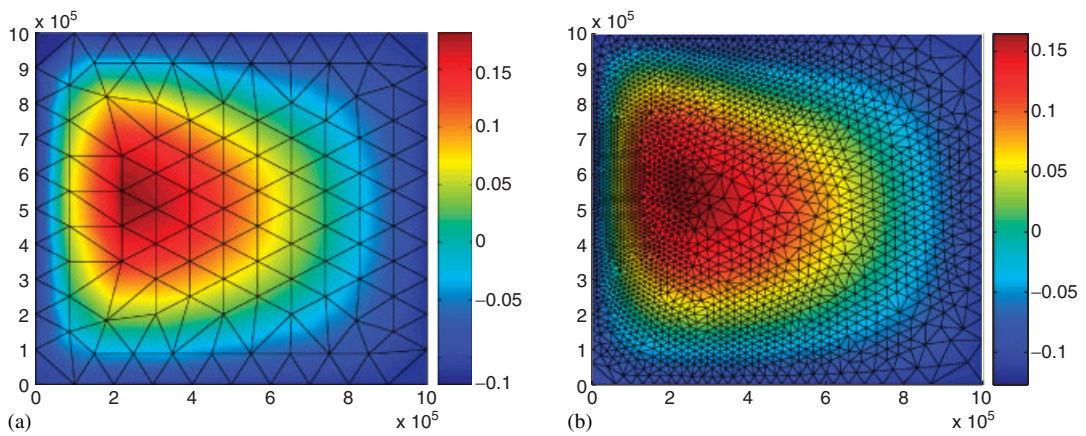

Figure 11. Nonlinear Stommel problem. The grid and color contours of the free surface for (a) an unstructured grid with $N_e = 206$ and (b) an adaptive unstructured grid with $N_e = 4608$ elements, both using $N = 1$ polynomials.

and Figure 12(b) is for an unstructured grid with 250 elements. The soliton wave is initially positioned at the origin and (according to the asymptotic solution) moves to $x = -15.70$ during the 40 time units. Furthermore, the asymptotic solution predicts that the maximum peak will be 0.1177. The results for the structured and unstructured grids give the same final position with the maximum peak values as 0.1170 and 0.1171 for the structured and unstructured grids, respectively. We can only claim a slight improvement in accuracy with the unstructured grid; however, the cost of the integration is lower since fewer elements (and total grid points) are used. Recall that while

DOI: 10.1002/fld

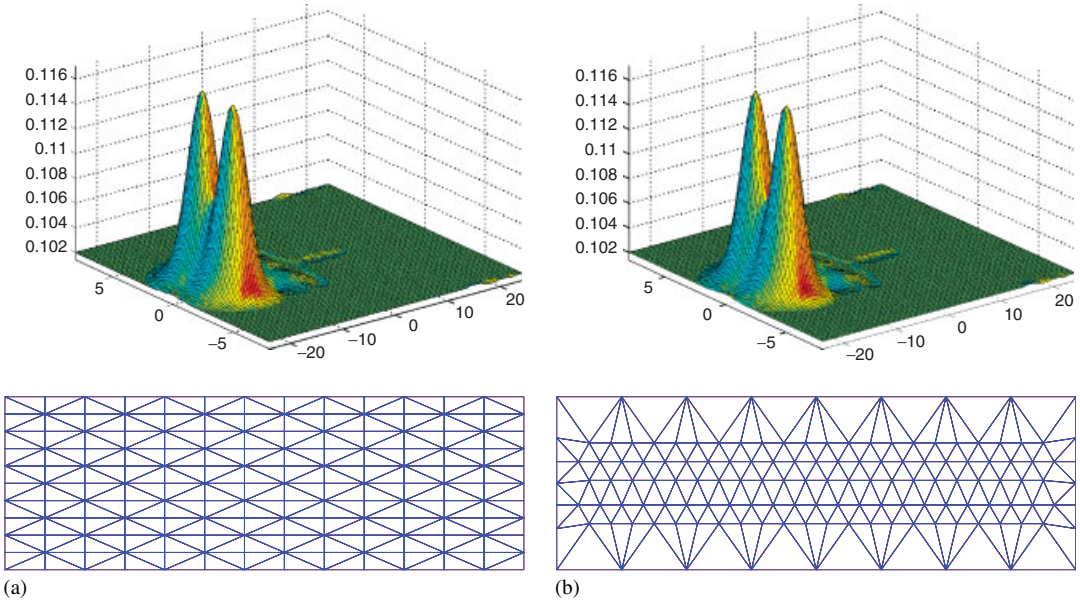

Figure 12. Nonlinear Rossby soliton wave. The free surface height and the linear grid for (a) the structured grid with $N_e = 260$ and (b) the unstructured grid with $N_e = 250$ elements, both using $N = 8$ polynomials.

the number of elements only differs by 10 for the two grids, the number of points, however, differs by 450.

5.4.4. Nonlinear Riemann problem. Figure 13 shows profiles of the free surface height along the x-axis for three different grids for the Riemann problem after 0.4 s; this is the final time at which the peak is at its maximum (see [37, Figure 13.12]). The grids shown in this figure are zoomed in such that the domain plotted is $(x, y) \in [-10, 10]^2$; note that the physical domain shown in the free surface height is $(x, y) \in [-20, 20]^2$. The plots in Figure 13(a) and (b) show results for structured grids with 20 000 and 80 000 elements, respectively. Figure 13(c) shows results for an adaptive grid using only 17 000 elements. Notice the undershoots at the base of the wave for both structured grids which are only slightly present in the adaptive grid. Furthermore, the maximum peak of the wave is approximately the same for both the structured grid with 80 000 elements and the adaptive grid with only 17 000 elements. The peak for the coarser structured grid is not only lower but the general shape of the wave is not as sharply defined. Admittedly, this specific problem lends itself quite easily to adaptivity because the wave only lies in a very small portion of the total domain and therefore an adaptive grid can capture this phenomenon quite well. However, our aim is using this technology for automatically refining the grid near islands and continental coastlines. This, we hope, will allow us to obtain highly resolved solutions near coastlines which has become an important topic for the modeling of tsunamis, storm surges, and hurricanes.

It should be mentioned that using a slope limiter will completely eliminate any nonphysical extrema from the solution. As an example, using the slope limiter presented in Section 3.6 will completely eliminate the oscillations from all three grids shown in Figure 13; these results are shown in Figure 14. There is little difference between the results using 80 000 structured elements

DOI: 10.1002/fld

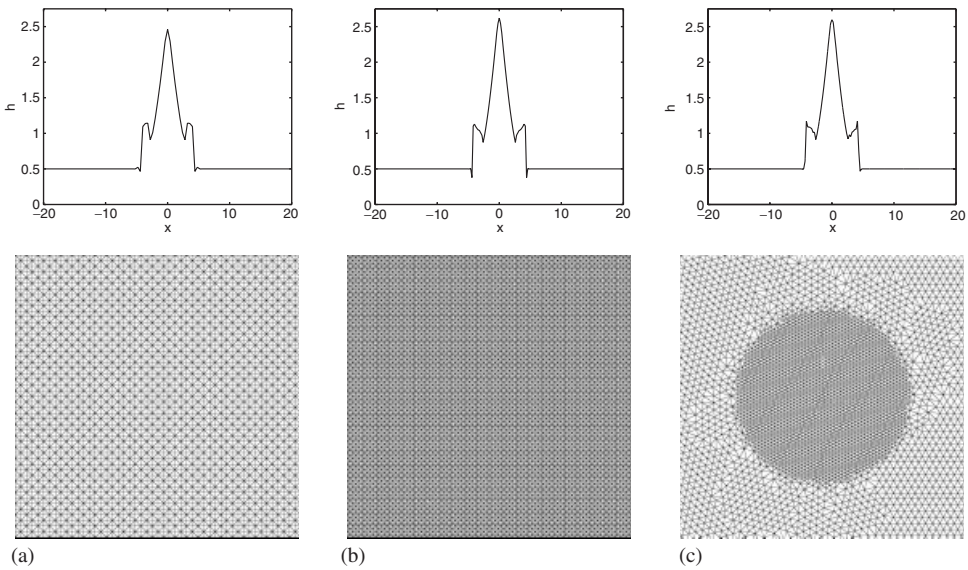

Figure 13. Riemann problem. Profile of the free surface height, h, along the x-axis and corresponding *zoomed* grid after 0.4 s for the DG model without slope limiting on (a) a structured grid with 20 000 elements ($n_r = 100$), (b) a structured grid with 80 000 elements ($n_r = 200$), and (c) an adaptive grid with 17 000 elements. All simulations use $N = 1$ polynomials.

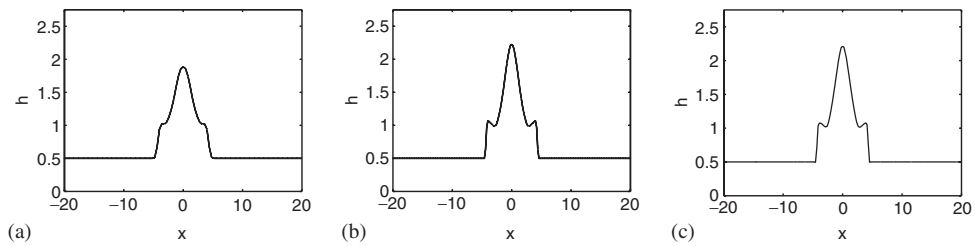

Figure 14. Riemann problem. Profile of the free surface height, h, along the x-axis after 0.4 s for the DG model with slope limiting on (a) a structured grid with 20 000 elements ($n_r = 100$), (b) a structured grid with 80 000 elements ($n_r = 200$), and (c) an adaptive grid with 17 000 elements. All simulations use $N = 1$ polynomials.

and those using the 17 000 adaptive elements; however, the results using 20 000 structured elements is clearly not as good. It should be pointed out that more sophisticated limiters exist in the literature which do not dampen the solution so strongly. We refer the interested reader to the papers by Cockburn and Shu [33] and Krivodonova *et al*. [32] where limiters are applied to low-order discontinuous Galerkin methods; unfortunately, the construction of quality slope limiters for high-order DG methods remains an open topic.

DOI: 10.1002/fld

6. CONCLUSIONS

We have presented a triangular nodal discontinuous Galerkin (DG) oceanic shallow water model that, although uses exact integration for the area and boundary integrals, needs no mass matrix. By imposing that the triangular elements be straight edged allows us to extract the metric terms from all the integrals. This then simplifies the algorithms considerably because one only needs to integrate on the reference element and then post-multiply the metric terms for each individual element; in addition, the mass matrix is absorbed into the basis functions which then eliminates it entirely from the equations. Another advantage of constraining the elements to be straight edged is that existing triangular mesh generators can be used quite easily with our DG model. While there have been other newly proposed DG shallow water models recently in the literature, the one we present here is the only one which uses a nodal approximation (i.e. it uses Lagrange polynomials rather than the modal approximations obtained with Jacobi polynomials) on the triangle. We chose the nodal approximation over the more common modal form to avoid mapping between spectral and physical space in order to facilitate the implementation of realistic boundary conditions when coupling this oceanic shallow water model with global ocean models. Furthermore, if the goal is to develop an accurate and efficient coastal ocean modeling tool, then the constraint of straight-edged triangles is not a limitation because one typically would need to assume this for constructing highly unstructured grids along detailed coastlines.

We showed results for six test cases, three of which have analytic solutions. The results showed that the DG model achieves exponential convergence up to 15th order (for $N = 14$). Furthermore, the comparisons with a spectral element (SE) model showed that the DG model yields more accurate solutions—often times two orders of magnitude better (for the linear standing wave and Stommel problem). A comparison of their relative efficiencies, however, should be performed. We showed results using slope limiters and adaptivity for the circular dam-break (Riemann) problem. The results obtained with the adaptive unstructured grid illustrated not only the ability of the DG method to handle discontinuities, but it also showed that a triangular DG method in combination with adaptivity can enhance the accuracy of discontinuous solutions.

The results obtained in this work encourage us to further develop this model. Future work will involve including viscous terms by virtue of the local discontinuous Galerkin method, slope limiters for high-order polynomials, dynamic grid adaptivity, and the construction of semi-implicit time integrators which will increase the efficiency of the model.

ACKNOWLEDGEMENTS

The first author (FXG) gratefully acknowledges the support of the Office of Naval Research through program element PE-0602435N. We would like to thank Emmanuel Hanert for sharing his Matlab code of the analytic solution for the linear Stommel problem.

REFERENCES

1. Arcas D, Titov V. Sumatra tsunami: lessons from modeling. *Surveys in Geophysics* 2006; **27**:679–705.
2. Walters R. A semi-implicit finite element model for non-hydrostatic (dispersive) surface waves. *International Journal for Numerical Methods in Fluids* 2005; **49**:721–737.
3. Schwanenberg D, Köngeter J. A discontinuous Galerkin method for the shallow water equations with source terms. In *Discontinuous Galerkin Methods*, Cockburn B, Karniadakis GE, Shu C-W (eds). Springer: Heidelberg, 2000; 289–309.

DOI: 10.1002/fld

4. Li H, Liu RX. The discontinuous Galerkin finite element method for the 2D shallow water equations. *Mathematics and Computers in Simulation* 2001; **56**:171–184.
5. Aizinger V, Dawson C. A discontinuous Galerkin method for two-dimensional flow and transport in shallow water. *Advances in Water Resources* 2002; **25**:67–84.
6. Dupont F, Lin CA. The adaptive spectral element method and comparisons with more traditional formulations for ocean modeling. *Journal of Atmospheric and Oceanic Technology* 2004; **21**:135–147.
7. Eskilsson C, Sherwin SJ. A triangular spectral/hp discontinuous Galerkin method for modelling 2D shallow water equations. *International Journal for Numerical Methods in Fluids* 2004; **45**:605–623.
8. Remacle JF, Frazão SS, Li XG, Shephard MS. An adaptive discretization of shallow-water equations based on discontinuous Galerkin methods. *International Journal for Numerical Methods in Fluids* 2006; **52**:903–923.
9. Kubatko EJ, Westerink JJ, Dawson C. hp discontinuous Galerkin methods for advection dominated problems in shallow water flow. *Computer Methods in Applied Mechanics and Engineering* 2006; **196**:437–451.
10. Giraldo FX, Hesthaven JS, Warburton T. Nodal high-order discontinuous Galerkin methods for the spherical shallow water equations. *Journal of Computational Physics* 2002; **181**:499–525.
11. Giraldo FX. High-order triangle-based discontinuous Galerkin methods for hyperbolic equations on a rotating sphere. *Journal of Computational Physics* 2006; **214**:447–465.
12. Ma H. A spectral element basin model for the shallow water equations. *Journal of Computational Physics* 1993; **109**:133–149.
13. Iskandarani M, Haidvogel DB, Boyd JP. A staggered spectral element model with application to the oceanic shallow water equations. *International Journal for Numerical Methods in Fluids* 1995; **20**:393–414.
14. Iskandarani M, Haidvogel DB, Levin JC. A three-dimensional spectral element model for the solution of the hydrostatic primitive equations. *Journal of Computational Physics* 2003; **186**:397–425.
15. Ozgokmen TM, Fischer PF, Duan JQ, Iliescu T. Three-dimensional turbulent bottom density currents from a high-order nonhydrostatic spectral element model. *Journal of Physical Oceanography* 2004; **34**:2006–2026.
16. Giraldo FX, Taylor MA. A diagonal mass matrix triangular spectral element method based on cubature points. *Journal of Engineering Mathematics* 2007; **56**:307–322.
17. Lynch DR, Ip JTC, Naimie CE, Werner FE. Comprehensive coastal circulation model with application to the Gulf of Maine. *Continental Shelf Research* 1996; **16**:875–906.
18. Ford R, Pain CC, Piggott MD, Goddard AJH, de Oliveira CRE, Umpleby AP. A nonhydrostatic finite element model for three-dimensional stratified oceanic flows. Part I: Model formulation. *Monthly Weather Review* 2004; **132**:2816–2831.
19. Anastasiou K, Chan CT. Solution of the 2D shallow water equations using the finite volume method on unstructured triangular meshes. *International Journal for Numerical Methods in Fluids* 1997; **24**:1225–1245.
20. Fringer OB, Gerritsen M, Street RL. An unstructured-grid, finite-volume, nonhydrostatic, parallel coastal ocean simulator. *Ocean Modelling* 2006; **14**:139–173.
21. Hesthaven JS. From electrostatics to almost optimal nodal sets for polynomial interpolation in a simplex. *SIAM Journal on Numerical Analysis* 1998; **35**:655–676.
22. Taylor MA, Wingate BA, Vincent RE. An algorithm for computing Fekete points in the triangle. *SIAM Journal on Numerical Analysis* 2000; **38**:1707–1720.
23. Proriol J. Sur une famille de polynomes á deux variables orthogonaux dans un triangle. *Comptes Rendus de l' Academie des Sciences Paris* 1957; **257**:2459.
24. Koornwinder T. Two-variable analogues of the classical orthogonal polynomials. In *Theory and Applications of Special Functions*, Askey R (ed.). Academic Press: San Diego, 1975.
25. Dubiner M. Spectral methods on triangles and other domains. *Journal of Scientific Computing* 1991; **6**:345–390.
26. Stroud AH. *Approximate Calculation of Multiple Integrals*. Prentice-Hall: Englewood Cliffs, NJ, 1971.
27. Cools R, Rabinowitz P. Monomial cubature rules since Stroud: a compilation. *Journal of Computational and Applied Mathematics* 1993; **48**:309–326.
28. Lyness J, Cools R. A survey of numerical cubature over triangles. *Applied Mathematics* 1994 **48**:127–150.
29. Cools R. Monomial cubature rules since stroud: a compilation. Part 2. *Journal of Computational and Applied Mathematics* 1999; **112**:21–27.
30. Kopriva DA. Metric identities and the discontinuous spectral element method on curvilinear meshes. *Journal of Scientific Computing* 2006; **26**:301–327.
31. Giraldo FX, Warburton T. A nodal triangle-based spectral element method for the shallow water equations on the sphere. *Journal of Computational Physics* 2005; **207**:129–150.
32. Krivodonova L, Xin J, Remacle JF, Chevaugeon N, Flaherty JE. Shock detection and limiting with discontinuous Galerkin methods for hyperbolic conservation laws. *Applied Numerical Mathematics* 2004; **48**:323–338.

DOI: 10.1002/fld

33. Cockburn B, Shu C-W. Runge–Kutta discontinuous Galerkin methods for convection-dominated problems. *Journal of Scientific Computing* 2001; **16**:173–261.
34. Stommel H. The westward intensification of wind-driven ocean currents. *Transactions of the American Geophysics Union* 1948; **29**:202–206.
35. Boyd JP. Equatorial solitary waves. Part 3: Westward-travelling modons. *Journal of Physical Oceanography* 1985; **15**:46–54.
36. Boyd JP. Equatorial solitary waves. Part 1: Rossby solitons. *Journal of Physical Oceanography* 1980; **10**: 1699–1717.
37. Toro E. *Shock-capturing Methods for Free-surface Shallow Flow*. Wiley: New York, 2001; 245.
38. Giraldo FX. A spectral element semi-Lagrangian method for the shallow water equations. *Fourth World Congress on Computational Mechanics*, CDROM, 1998.
39. Giraldo FX. Semi-implicit time-integrators for a scalable spectral element atmospheric model. *Quarterly Journal of the Royal Meteorological Society* 2005; **131**:2431–2454.
40. Cockburn B, Shu C-W. The local discontinuous Galerkin method for time-dependent convection–diffusion systems. *SIAM Journal on Numerical Analysis* 1998; **35**:2440–2463.
41. Behrens J, Rakowsky N, Hiller W, Handorf D, Läuter M, Päpke J, Dethloff K. AMATOS: parallel adaptive mesh generator for atmospheric and oceanic simulation. *Ocean Modelling* 2005; **10**:171–183.
42. Giraldo FX. A space marching adaptive remeshing technique applied to the 3D Euler equations for supersonic flow. *Ph.D. Thesis*, University of Virginia, 1995.
43. Giraldo FX. The Lagrange–Galerkin method for the two-dimensional shallow water equations on adaptive grids. *International Journal for Numerical Methods in Fluids* 2000; **33**:789–832.

DOI: 10.1002/fld